Electronic structure and vibrational stability of copper-substituted lead apatite LK-99

J. Cabezas-Escares◉ and Nicolás F. Barrera◉

Departamento de Física, Facultad de Ciencias, Universidad de Chile, Santiago 7800024, Chile
and Center for the Development of Nanoscience and Nanotechnology, Santiago 9330111, Chile

Robert H. Lavroff◉

Department of Chemistry and Biochemistry, University of California, Los Angeles, California 90095, USA

Anastassia N. Alexandrova◉

Department of Chemistry and Biochemistry, University of California, Los Angeles, California 90095, USA;
Department of Materials Science and Engineering, University of California, Los Angeles, California 90095, USA;
and California NanoSystems Institute, University of California, Los Angeles, California 90095, USA

C. Cardenas and F. Munoz◉*

Departamento de Física, Facultad de Ciencias, Universidad de Chile, Santiago 7800024, Chile
and Center for the Development of Nanoscience and Nanotechnology, Santiago 9330111, Chile

Two recent preprints [Lee *et al.*, arXiv:2307.12008 and Lee *et al.*, arXiv:2307.12037] have received attention because they claim experimental evidence that a Cu-substituted apatite material (dubbed LK-99) exhibits superconductivity at room temperature and pressure. If this proves to be true, LK-99 will be a holy grail of superconductors. In this work, we use density functional theory $+ U$ calculations to elucidate some key features of the electronic structure of LK-99. We find two different phases of this material: (i) a hexagonal lattice featuring metallic half-filled and spin-split bands, nesting of the Fermi surface, and a remarkably large electron-phonon coupling that is vibrationally unstable and (ii) a triclinic lattice, with the Cu and surrounding O distorted. This lattice is vibrationally stable, and its bands correspond to an insulator. In a crystal, the Cu atoms should oscillate between equivalent triclinic positions, with an average close to the hexagonal positions. We discuss the electronic structure expected from these fluctuations and whether it is compatible with superconductivity.

I. INTRODUCTION

Since the discovery of superconductivity in 1911 by Onnes [1,2], the phenomenon has fascinated scientists. Many efforts have been made to find materials capable of this property under conditions of temperature and pressure that allow practical applications. This search has resulted in the discovery of materials such as the conventional, or BCS, superconductor MgB_2 with $T_c = 39$ K [3] and unconventional (beyond BCS) superconductor Y-Ba-Cu-O [4] ($T_c = 93$ K). Nevertheless, a room-temperature and -pressure superconductor remains elusive.

The material dubbed LK-99, an apatite-like crystal with the approximate formula unit $CuPb_9(PO_4)_6O$, has recently been in the spotlight of the condensed matter physics community, as two articles claim it has a superconducting critical temperature over 400 K at atmospheric pressure [5,6]. If these claims prove to be true, this discovery could be a major advancement in the field of superconductivity.

Most of the recent literature on this material points against it being a superconductor, with several apparently successful replication attempts capable of reproducing results such as x-ray patterns but without exhibiting superconductivity [7–10]. It now seems generally accepted that the abrupt drop in electrical resistance below $T = 104\,°C$ originates from CuS_2 impurities [11–17]. Interestingly, one study found that CuS_2 impurities cannot reproduce the colossal magnetoresistance at room temperature found in LK-99 [18], so this material could be promising as a magnetic sensor. An experimental study described a strange metal phase in this system without discarding the observation of the Meissner effect [19]. Another study suggested the possibility of interfacial superconductivity at grain boundaries [20]. A theoretical paper supported this last idea, with a model of excitonic superconductivity [21]. Recent theoretical studies focused on understanding the defects contained in this material or its parent compounds [22,23] and the structural stability of the crystal structure associated with LK-99 [24–26]. One theoretical study has even shown that this material could be one of the few that hosts Weyl fermions while breaking time-reversal symmetry [27].

In this article, we explore the possibility of LK-99 being such a superconducting material.

We will begin by discussing in Sec. II the main properties and crystal structure of lead apatite. Then, in Sec. III we will

*fvmunoz@gmail.com

elaborate on the possible crystal structure and magnetic order of the so-called LK-99 system, as well as its electronic structure. This is the structure we saw in other theoretical studies [23,28–39], and we will show it is vibrationally unstable. In Sec. IV we will introduce a related crystal structure that does not have imaginary phonon frequencies but is a band insulator. We will discuss our findings in Sec. V. Finally, we will close this contribution with our conclusions in Sec. VI.

II. LEAD APATITE

Lead apatite materials have a hexagonal lattice with space group $P6_3/m$ and formula unit $Pb_{10}(PO_4)_6X_2$, with $X=$Cl, OH, F, Br [40]. However, the apatite-like LK-99 phase has a slightly different composition, $Pb_{10-x}Cu_x(PO_4)_6O$. There are reports of a related (Ca-based) oxyapatite crystal with the desired composition [41]. Its crystal structure is very close to other apatite materials. It has a hexagonal lattice with space group 174 and point group $P\bar{6}$. We used this geometry as our basis to computationally characterize Pb apatite, $Pb_{10}(PO_4)_6O$. We obtain lattice parameters $a = 10.00$ Å and $c = 7.44$ Å, which are slightly larger than experimental reports of similar systems [42,43]. Theoretical works with similar methods show close [30], slightly smaller [26], or even larger cells [44]. However, after including Cu atoms, the differences in lattice parameters among theoretical studies are minimal. The geometry used is shown in Fig. 1(a), with Pb atoms forming hexagonal patterns, as shown in Fig. 1(b). This Pb apatite is predicted to be an insulator, as can be seen from its band structure diagram [see Fig. 1(c)]. A more sophisticated hybrid exchange-correlation (XC) functional, HSE06 [70], gives a band gap of ~3.8 eV (see Sec. VII). The conventional lead hydroxyapatite, $Pb_{10}(PO_4)_6(OH)_2$, has a similar band structure but a larger band gap.

III. LK-99: HEXAGONAL LATTICE

A. Crystal structure

According to Lee *et al.* [5,6], the LK-99 phase has the formula unit $Pb_{10-x}Cu_x(PO_4)_6O$, with $0.9 < x < 1.1$, with Cu atoms replacing a specific Pb sublattice [the green atoms in Figs. 1(a) and 1(b)]. For simplicity, we set $x = 1$, i.e., a single Cu atom per unit cell. This substitution Pb → Cu implies an odd number of electrons per unit cell, suggesting a metal with a spin-split ground state or a doubling of the unit cell. Figure 2 shows two possible arrangements when doubling the unit cell along the c axis, denoted stackings A and B. In stacking A (B) the Cu atoms form a triangular (hexagonal) sublattice. The space group of stacking A (B) is 174 (143).

Overall, six possible arrangements are considered: stacking sequences A and B, each with a ferromagnetic (FM), antiferromagnetic (AFM), or nonmagnetic (NM) ground state. In the AFM stacking, the in-plane spins are parallel with an antiparallel out-of-plane order. The relative energies, without including any Hubbard-like U electron-electron repulsion correction, are given in Table I. It is evident that a magnetic order is preferred over NM. Also, stacking A (triangular Cu sublattice) is slightly more stable than stacking B. The energies of all the different magnetic orders being almost the same is the first hint that the Cu atoms do not form extended states. A caveat is
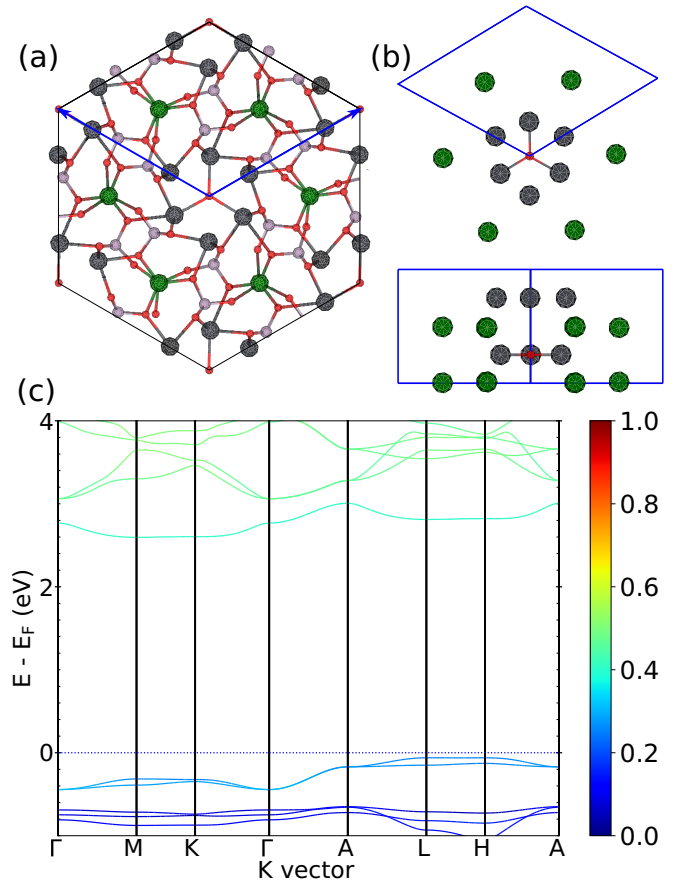

FIG. 1. (a) In-plane view of the crystal structure of lead apatite, $Pb_{10}(PO_4)_6O$. Nonequivalent Pb atoms are colored gray and dark green. O is red, and P is pink. The lattice vectors are blue arrows. (b) Top and side views of the two hexagonal-like patterns formed by Pb atoms. The inner hexagonal pattern has three Pb atoms in different layers; these layers are not equivalent since one of them has an O at its center. (c) Band structure of lead apatite. The color intensity reflects the projection of the wave functions onto Pb atoms (i.e., within its Wigner radius).

that the designation as FM and AFM is questionable due to the absence of an effective exchange interaction among Cu atoms preventing a long-range magnetic order (i.e., in a Heisenberg model, the exchange parameters should be practically zero); however, it is relevant to include spin polarization to correctly describe the system.

We tested the effect of a Hubbard-like term $U = 2.0$ eV on the relative energy of stacking A for the NM and FM orders, and the results are similar to those in Table I, with the NM order being 0.18 eV/f.u. higher in energy than the FM order. This larger stability of the spin-split state is expected from the addition of electron-electron interaction.

B. Electronic properties

Given the larger stability of stacking A (triangular Cu sublattice; see Fig. 2), we calculated its band structure. In the NM and FM cases, the unit cell of $Pb_9Cu_1(PO_4)_6O$ suffices to describe the system (i.e., no supercell is needed). Figure 3 shows the band structure of the FM order. Two Cu
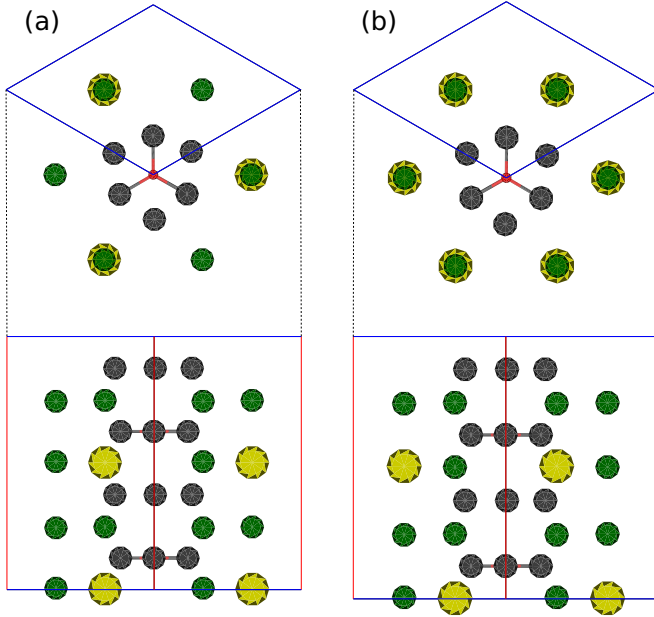
FIG. 2. Possible LK-99 atomic structures. The unit cell of lead apatite was duplicated along the c axis. To keep the figure as simple as possible, P and most O atoms are omitted. The Cu atoms are yellow and large. (a) and (b) show two possible stacking sequences, A and B, with Cu atoms forming a triangular or hexagonal sublattice.

d orbitals form almost flat bands at the Fermi level: their width is ≈ 0.1 eV [see Fig. 4(a)]. These bands are half filled, and the system is metallic. These bands are very similar to other reports, with $U = 4$–7 eV, with and without spin-orbit interaction [28–31,32,34,36,37]; see Appendix E for the effect of changing the value of U.

The Fermi surface and other isovalues of the bands are shown in Figs. 4(b)–4(d). Here a nesting of the Fermi surface seems likely: two bands have an almost spherical shape, but one is centered at Γ, and the other is centered at A. Fermi nesting is often associated with a charge density wave [45], as suggested by the original preprint attempting to explain the superconductivity of LK-99 [6]. However, the link between nesting and a charge density wave is the Peierls distortion or a related mechanism [46]. This mechanism can induce some other effects, including an actual change in geometry, such as dimerization. In fact, there are theoretical arguments to expect a reduction in the symmetry of the system [47]. A deeper

TABLE I. Relative energies of different stackings and magnetic orders of $Pb_9Cu_x(PO_4)_6O$. The minimum energy configuration is taken as zero. These are the only results with the Hubbard-like term $U = 0$ in the article. The units are eV/f.u.

	Stacking/spin	
	A	B
NM	0.13	0.17
FM	0.00	0.02
AFM	0.00	0.04

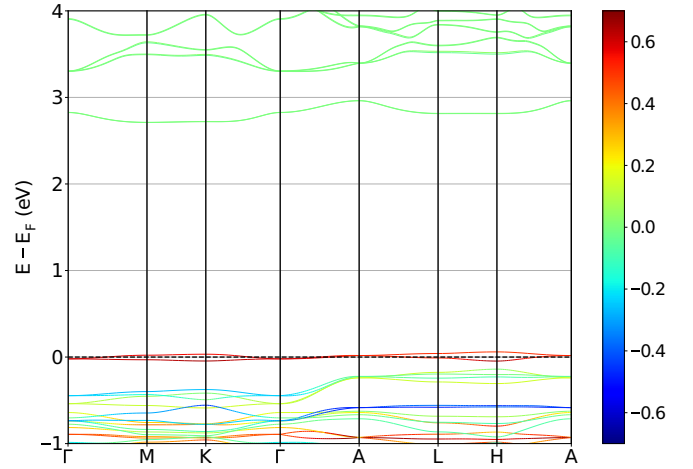
FIG. 3. Band structure of $Pb_9Cu_1(PO_4)_6O$ with stacking A and a FM ground state. The color scale represents the projection of wave functions onto the Cu atom, where a positive or negative value denotes the spin value.

discussion, including the possible nesting vector, is provided in Appendix A.

The electron localization function (ELF) is large in those regions of space where we are likely to find electron pairs of opposite spin [48]. Hence, the ELF is large in regions associated with covalent chemical bonds, lone pairs of electrons, and the inner shells of atoms. Contour plots of the ELF along planes containing the Cu atoms (see Fig. 5) suggest that Cu is not strongly covalently bonded to its neighbor oxygen atoms. Indeed, the shape of the ELF around Cu resembles that of atoms confined in wells [49,50]. This observation is consistent with the slight hybridization of the d and s orbitals of Cu with the p orbitals of oxygen, as shown by the angular
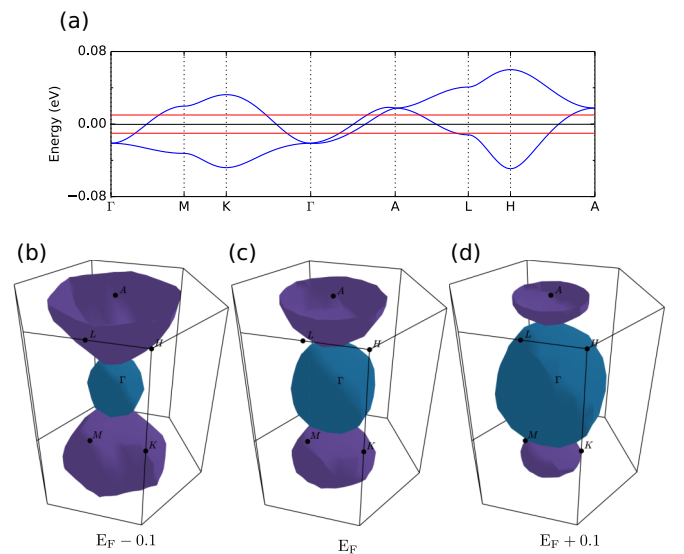

FIG. 4. (a) Zoom of the bands at the Fermi level. Isosurfaces of the bands at (b) $E_F - 0.01$ eV (E_F is the Fermi energy), (c) E_F, and (d) $E_F + 0.01$ eV. Different bands are in different colors; the two spherical-like surfaces, centered and Γ and A, are apparently nested.
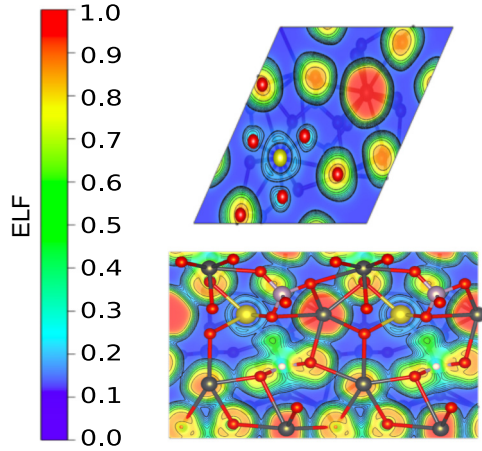
FIG. 5. Contour plots of the ELF (dimensionless) on planes that cross the Cu atoms and are parallel to (1,0,0) (bottom) and (0,0,1) (top). The coloring of the atoms follows Figs. 1 and 2; i.e., the Cu atom is yellow.
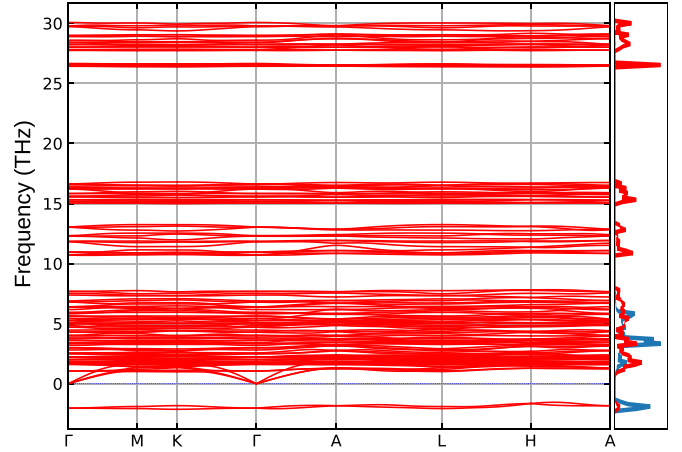

FIG. 6. Phonon band structure of arrangement A (triangular Cu sublattice, space group 174). The right panel shows the total (red) and partial (Cu projection, blue) phonon densities of states.

momentum decomposition of the density of states of the Cu atom (see Fig. 15 in Appendix D). A better understanding of the bonding of Cu may benefit from including static correlation in the bonding analysis, such as in the hybridization function [51,52], but that is beyond the scope of this study.

Interestingly, Belli *et al.* [53] found an empirical positive correlation between the critical temperature of a high-pressure-hydrogen-based superconductor and what they called the networking value, ϕ, of the ELF. ϕ is "the highest value of the ELF that creates an isosurface spanning through the whole crystal in all three Cartesian directions." If these criteria were to apply to LK-99, its critical temperature would be less than 50 K (see Fig. 4 in [53]). It is worth noting that the quality of the ELF is only as good as its underlying density functional theory (DFT) calculations, so its interpretation should be taken with a grain of salt.

C. Phonons and electron-phonon coupling

At the harmonic level, the phonon band structure of arrangement A (see Fig. 6) has well-defined groups of bands, including two completely imaginary branches. These branches indicate that the geometry with group 174 is dynamically unstable, at least under the conditions of our calculations. In Sec. IV, we will explore a related but vibrationally stable structure. Anharmonic effects were studied elsewhere [25], and we will discuss them in Sec. V A

Other features of the phonons include (1) the absence of dispersive phonons, indicating that the system is constructed from molecularlike blocks, and (2) the displacement of Cu atoms being confined to low-energy phonons (up to 30 meV), falling within the energy width of the Cu bands at the Fermi level. More energetic modes involve the rearrangement of O atoms surrounding the Cu.

Ignoring the imaginary frequencies, it could be instructive to have a crude idea about the electron-phonon coupling (EPC) of the system. The degenerate flat bands at the Fermi level imply a potentially large EPC. Its evaluation with DFT

is highly expensive, especially for such a large unit cell, and EPC within the generalized gradient approximation (GGA) + U is not included in the DFT codes known to us. Nevertheless, we have adopted a much simpler approach to obtain insights into how large the EPC could be.

According to the isotropic Migdal-Eliashberg theory [54], the overall EPC is a weighted integral of the $\alpha^2 F(\omega)$ function, which adds all the electron-phonon matrix elements $|g_{mn\nu}(\mathbf{k}, \mathbf{q})|^2$ compatible with momentum and energy conservation at the Fermi level. Explicitly,

$$g_{mn\nu}(\mathbf{k}, \mathbf{q}) = \langle u_{m,\mathbf{k}+\mathbf{q}} | \Delta_{\mathbf{q}\nu} v^{\text{KS}} | u_{n,\mathbf{k}} \rangle, \tag{1}$$

where $\mathbf{k}$ and $\mathbf{q}$ refer to electron and phonon momenta, respectively. m and n are electronic band indexes, and ν is a phonon index. $u_{n\mathbf{k}}(r)$ is the lattice-periodic part of the wave function, and v^{KS} is the Fourier transformed Kohn-Sham potential. $\Delta_{\mathbf{q}\nu}$ indicates the (first-order) changes in the potential due to phonon $\mathbf{q}$ of branch ν.

In short, a prerequisite for a large EPC is large matrix elements $g_{mn\nu}$. This is particularly relevant in the case of LK-99, for which only two electronic bands are relevant. They correspond to the d_{xz} and d_{yz} orbitals [28]. These orbitals are nearly degenerate (see Fig. 4), leading us to anticipate the most substantial effect when a phonon disrupts the degeneracy between these orbitals. Although the lifting of a degeneracy does not invariably result in a large EPC, it does occur in certain systems, such as MgB_2. In this system, lattice phonons that split the degeneracies along the Γ-A line are the most influential [55,56]. It is important to note, however, that MgB_2 and LK-99 are very different systems [57], and this example is used solely to highlight the potential impact of lifting a degeneracy on $g_{nm\nu}$. This mechanism has also been used to explain the larger critical temperature of YB_6 with respect to nearly identical LaB_6 [58].

The effect of such a frozen phonon is dramatic (see Fig. 7). Not only is the degeneracy lifted along Γ-A, but one of the d bands is now buried $\sim$0.5 eV below E_F for every point of reciprocal space. These changes notably turn LK-99 into an insulator. We are unaware of any similar effect in other materials. It is worth commenting on a similar approach
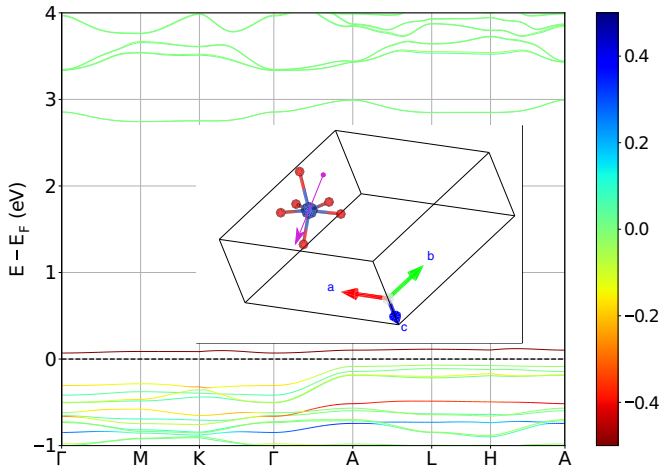
FIG. 7. Band structure of LK-99 under the distortion from a frozen phonon. The color scale shows the projection of the wave function onto the Cu atom; the positive (negative) values denotes the majority (minority) spin. The inset shows the actual phonon at Γ with a purple arrow. It is mostly localized in the Cu atom (blue). The d orbitals are no longer degenerate, with one of them buried $\sim$0.5 eV below E_F (red-orange band). The amplitude of the frozen phonon was 0.04Å, mostly involving a shift of the Cu atom from its equilibrium position [59].

involving frozen phonons with a larger amplitude, which was used in MgB_2 (see Fig. 3 of Ref. [55]) to shed light on the EPC due to the E_{2g} phonons and similarly to predict a BCS superconductor with a large EPC [60]. In both cases, a splitting of degenerate bands of about $\sim$2 eV was observed. However, they continued to be metals.

IV. LK-99: TRICLINIC LATTICE

A. Crystal structure and phonons

By following the distortion associated with one of the imaginary phonon branches (with zero momentum, the Γ point) we obtained a crystal structure of $Pb_9Cu(PO_4)_6O$ stable
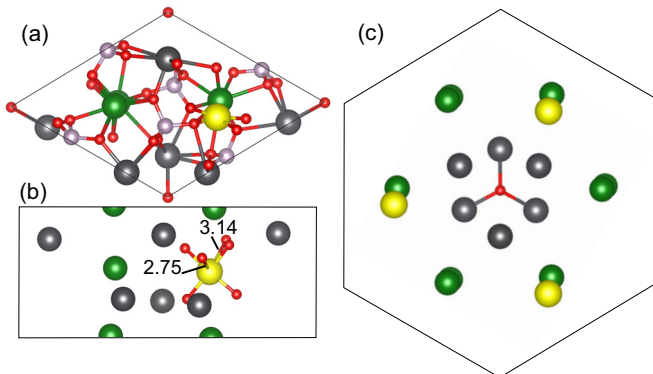

FIG. 8. (a) Unit cell of the triclinic $Pb_9Cu_1(PO_4)_6O$ obtained after relaxation. (b) Lateral view, with emphasis on the O atoms closer to Cu. The distances shown are in angstroms, and the other distances are very close to 2.0 Å. (c) Top view, removing atoms other than Cu, Pb, and the central O. The colors follow Fig. 1; Cu is yellow.
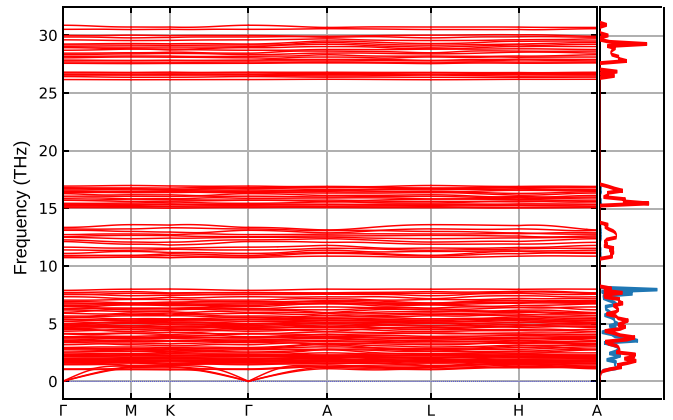

FIG. 9. Phonon band structure for the triclinic LK-99-like crystal structure. The right panel shows the total (red) and partial (Cu projection, blue) phonon densities of states.

at the harmonic level, with a triclinic lattice and space group 1 (see Fig. 8). It is very close to a hexagonal lattice [see Fig. 2(a)]. Since the atomic rearrangements are centered in the Cu atom, we predict that (1) following the same phonon with a different momentum plus an adequate supercell should result in different final geometries and (2) following the other imaginary phonon branch should yield a result similar to the one obtained, related by a symmetry operation. In a large system, both types of distortion could coexist, and studying them in a unit cell is unrealistic. The triclinic unit cell is 0.55 eV/f.u. lower in energy than the hexagonal one. Even though this value may seem large, it is only 13 meV per atom. We do not study different magnetic arrangements in this section.

The phonon band structure of the triclinic system has no imaginary branches (see Fig. 9). Otherwise, it has the same features as the hexagonal lattice.
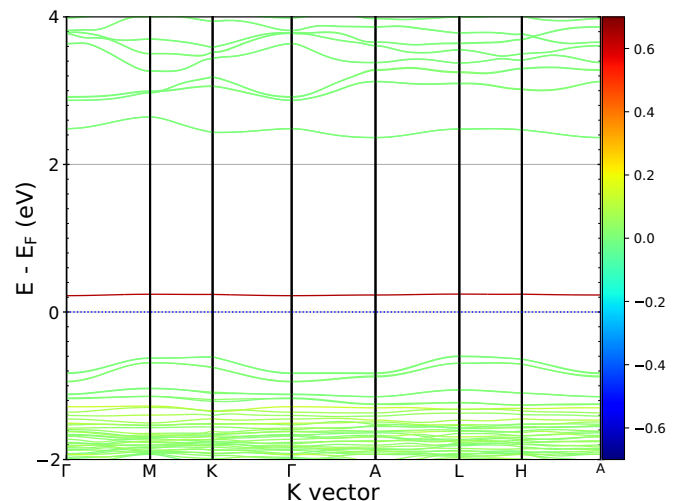

FIG. 10. Band structure of the LK-99-like system with the triclinic lattice. The color scale shows the projection of the wave function onto the Cu atom; the positive (negative) values denote the majority (minority) spin. There is a single band within the fundamental band gap; it is not spin degenerate.
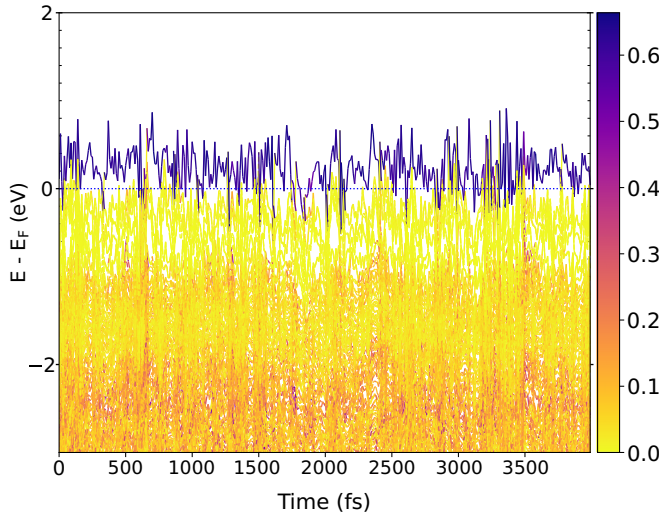
FIG. 11. Energy levels at Γ of a unit cell of $Pb_9Cu(PO_4)_6O$ at room temperature. The color intensity is the projection of each wave function on Cu atoms.

B. Electronic structure

The triclinic system's band structure (Fig. 10) resembles that of our frozen phonon calculation (Fig. 7) and a recent study [61]. This is not surprising since in the hexagonal lattice, the degeneracy along Γ-A and the Fermi surface nesting suggest a Jahn-Teller-like distortion lowers the total energy [47].

Regarding superconductivity, the lowest energy structure of apatite-like $Pb_9Cu(PO_4)_6O$ is an insulator. However, a small electron doping (e.g., defects) should turn the system into a metal.
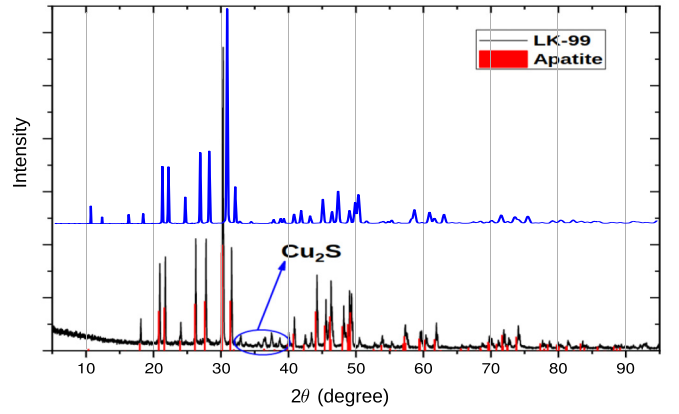

FIG. 13. XRD of LK-99 obtained in this work (blue line). For comparison, Fig. 2 of [5] is included (black and red lines).

V. DISCUSSION

We have studied two Cu-doped lead apatite systems with hexagonal and triclinic lattices. The hexagonal lattice has promising electronic properties for superconductivity, but it is not stable against vibrations (at the harmonic level). The triclinic system has the lowest energy and is vibrationally stable; however, it is a band insulator. Now, we are in a position to comment on two relevant questions.

A. What is the actual crystal structure of LK-99?

Does the LK-99 material assume the hexagonal or the triclinic lattice? We are convinced the picture is not so simple, even assuming the simplest stoichiometry $Pb_9Cu(PO_4)_6O$. Even at low temperatures of ~60 K, the system should fluctuate between the different symmetry-related distortions, resulting in a larger effective symmetry than the triclinic
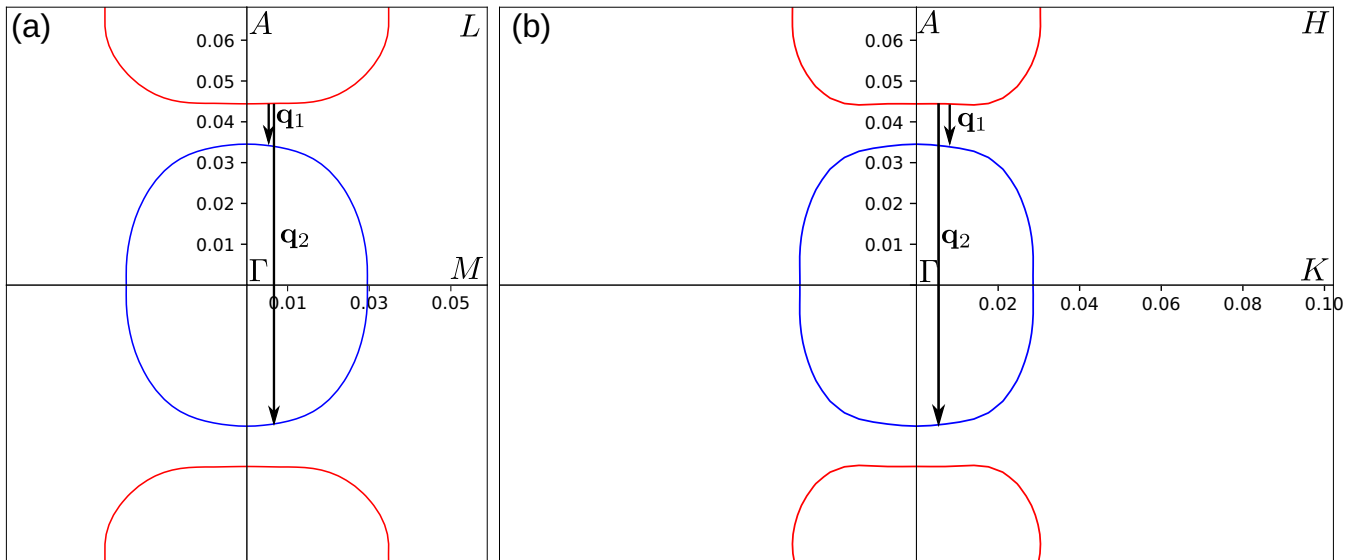

FIG. 12. Two-dimensional contour plots of the Fermi surface of the hexagonal lattice of LK-99. The bands are those plotted in Fig. 4. (a) and (b) show different planes. The arrows represent a pair of phonons with momenta $\mathbf{q}_1$ and $\mathbf{q}_2$ connecting two Fermi surfaces. The length of the arrow is the same in both panels.

FIG. 15. Projected density of states on the Cu atom in LK-99 with stacking A and an FM ground state. Labels $p/3$ and $d/5$ indicate that the sum of the PDOS is divided by 3 and 5, respectively.
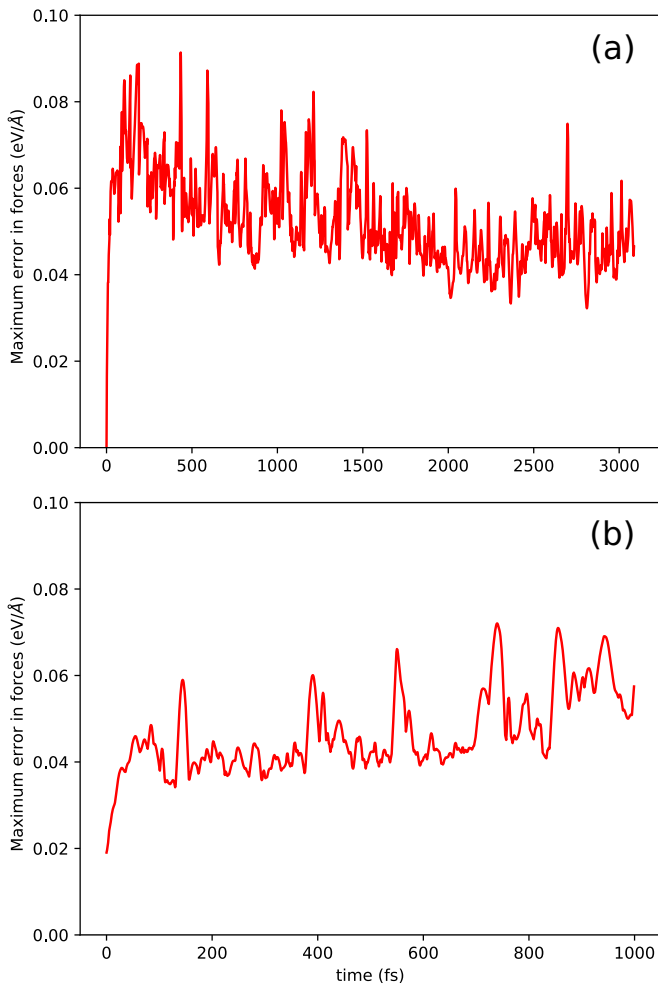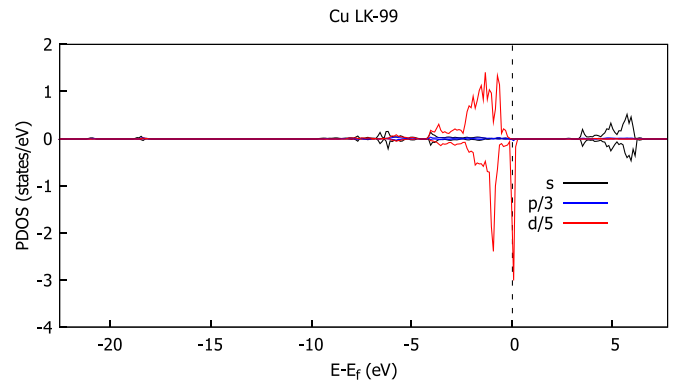

FIG. 14. Bayesian estimation of the error on the forces, or statistical uncertainty. Only the largest error for each time step is plotted. (a) Fitting the force field by mixing DFT and the force field, the plot corresponds to the last refinement of the force field. (b) Molecular dynamics of a $3 \times 3 \times 3$ supercell at room temperature, using only the force field.

system. In our study we neglected anharmonic contributions, but they might be able to stabilize the hexagonal structure at high enough temperature. Indeed, recently, a preprint showed that anharmonic effects remove the imaginary phonon branches of the hexagonal structure at room temperature [25]. In Appendix B, we calculate the average x-ray diffraction (XRD) pattern along a molecular dynamics simulation, which agrees with a thermal stabilization of the hexagonal lattice.

On top of the previous discussion, we need to mention that we are unaware of any successful replication of the crystal up to now, at least as proposed in the original preprints. Experimental samples suffer from Cu clustering [62], as evidenced by the inhomogeneous magnetism [13].

B. Is LK-99 a superconductor?

From the previous discussion, a BCS superconducting state is unclear. Unless the crystal has a perfect hexagonal lattice, the system should be a band insulator. Let us assume the flat band of Fig. 10 is half occupied (which it is not); the EPC

should not induce large changes in the electronic structure. The band is flat (atomiclike) and should remain so, unless another Cu d orbital gets close in energy, returning to something like the hexagonal crystal (i.e., nearly degenerate half-filled bands; see Fig. 3). In BCS superconductors, usually, the EPC splits degenerate bands instead of inducing degeneracies.

Even if the hexagonal lattice is stable at room temperature [25], its electronic structure at room temperature could be different from the two-flat-band picture in Figs. 3 and 4. To get some insight into the electronic structure of this material at room temperature, we carried out a DFT-based molecular dynamics (MD) simulation of one unit cell. Figure 11 shows the energy levels as a function of time. Since the bands of interest are very flat, we plot only the values at Γ. In Fig. 11, the bands are colored according to their projection onto Cu atoms. Along most of the dynamics, only one Cu-like level exists close to the Fermi level. The next Cu level lies about 1 eV below the Fermi level, and it is hybridized with other atoms (pale purple stripe). Only at $t \approx 3500$ fs are two Cu bands at the Fermi level, making it an infrequent event. Despite the finite-size errors from our MD simulations, we are confident that the two-flat-band picture does not hold at room temperature. Then we can discard the idea that the system is a high-temperature superconductor, even if it is doped to be metallic. Of course, if the experimental crystal structure differs from the one calculated here (e.g., Cu clustering and Cu atoms in nonequivalent lattice positions), this analysis would need to be reassessed.

VI. CONCLUSIONS

The so-called LK-99 material is a Cu-doped lead oxyapatite system. We studied specifically the system $Pb_9Cu(PO_4)_6O$ with two possible crystal structures: a hexagonal lattice and a triclinic lattice.

The hexagonal lattice has attracted much attention, and it features practically flat, half-filled bands. They are spin split. The Fermi surfaces show a nesting around Γ and A. These bands are unstable against vibrations (i.e., imaginary phonon frequencies) at least at the harmonic level.

By following one of the imaginary phonon branches, we found a very similar triclinic lattice. It is lower in energy
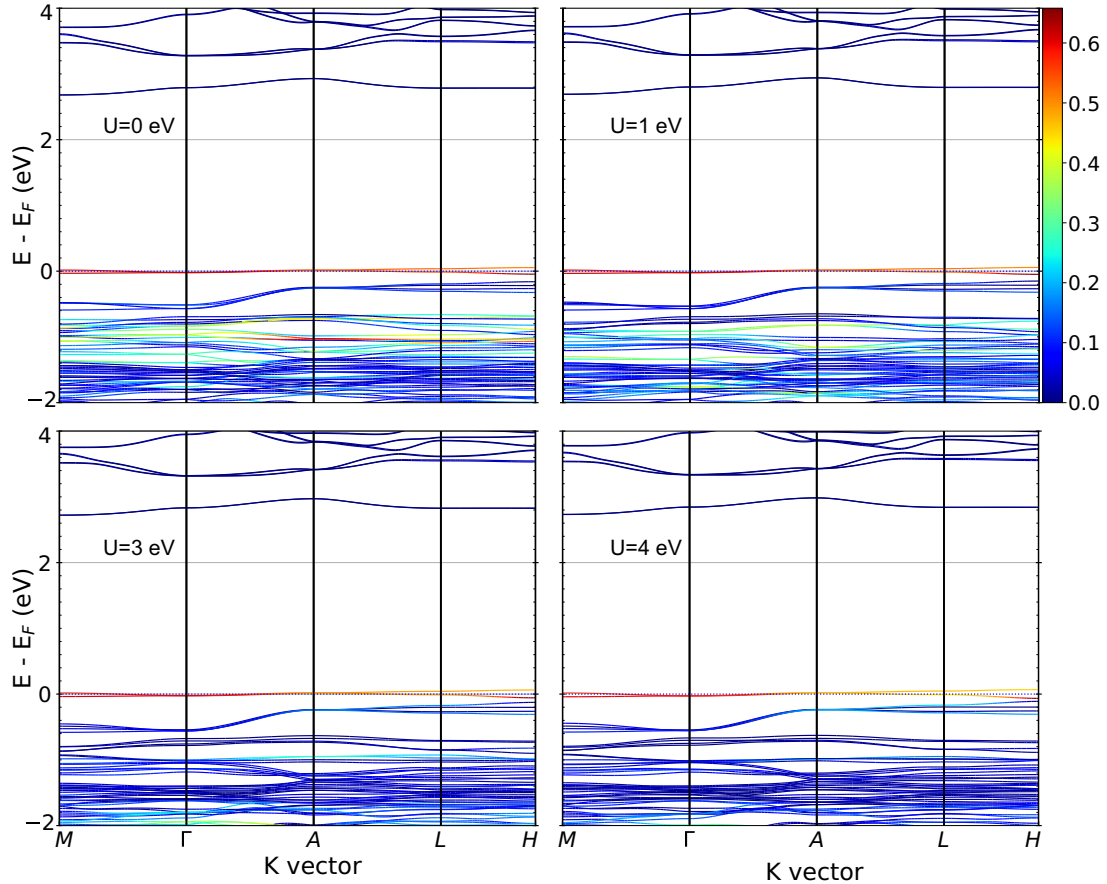
FIG. 16. Band structure of the hexagonal lattice phase of LK-99 of some values of the Hubbard-like term U. The color bar denotes the projection of Cu atoms onto the state.

and vibrationally stable. However, it is a band insulator, with a single spin-split unoccupied band within the fundamental band gap.

Since the energy barrier between both lattices is much smaller than room temperature, in a crystal the Cu atom should oscillate between the different phases, giving an overall symmetry larger than triclinic. Along these oscillations insulating and metallic states could take place. However, having half-filled, almost flat bands is an infrequent event.

A superconductor is unlikely, at least from the BCS picture. If the material is a superconductor, its crystal structure probably differs from the one being reported.

VII. COMPUTATIONAL METHODS

We employed DFT as implemented in the VASP package [63–66] using the projector augmented wave method [67] and Perdew-Burke-Ernzerhof (PBE) XC functional [68]. For the lead apatite we made some calculations with the HSE06 hybrid functional [69–71], but since all relevant physics is captured by simpler methods, we kept PBE throughout the article. To ensure the completeness of the basis, we set the energy cutoff to 520 eV. In the structural optimization, the k-point grid was set to $3 \times 3 \times 4$. The smearing used for k-point integration was 10 meV.

For phonon calculations, we used a classical force field created with machine learning of a DFT molecular dynamics

simulation [72,73]. We used a supercell of size $3 \times 3 \times 3$. The PHONOPY [74–76] software was employed for the postprocessing of phonons. The mesh for the phonon density of states was set to $10 \times 10 \times 10$. More details about the force field generation are given in Appendix C.

PYPROCAR [77,78] was employed for analyzing the electronic structure. The IFERMI [79] software was used to plot Fermi surfaces. Unless otherwise stated in the text, the calculations used the GGA + U approach in the rotationally invariant scheme of Dudarev *et al.* [80]. We used a value of $U = 2.0$ eV for the d orbitals of Cu. Electronic band structures without this correction or with a different value are qualitatively similar (see Appendix E).

To build the crystal structure of LK-99, we used as a starting point the crystal structure of apatite available on the Materials Project website [81]. Then the composition was adjusted to that of LK-99, and the cell was fully relaxed. Structures were built with VESTA [82].
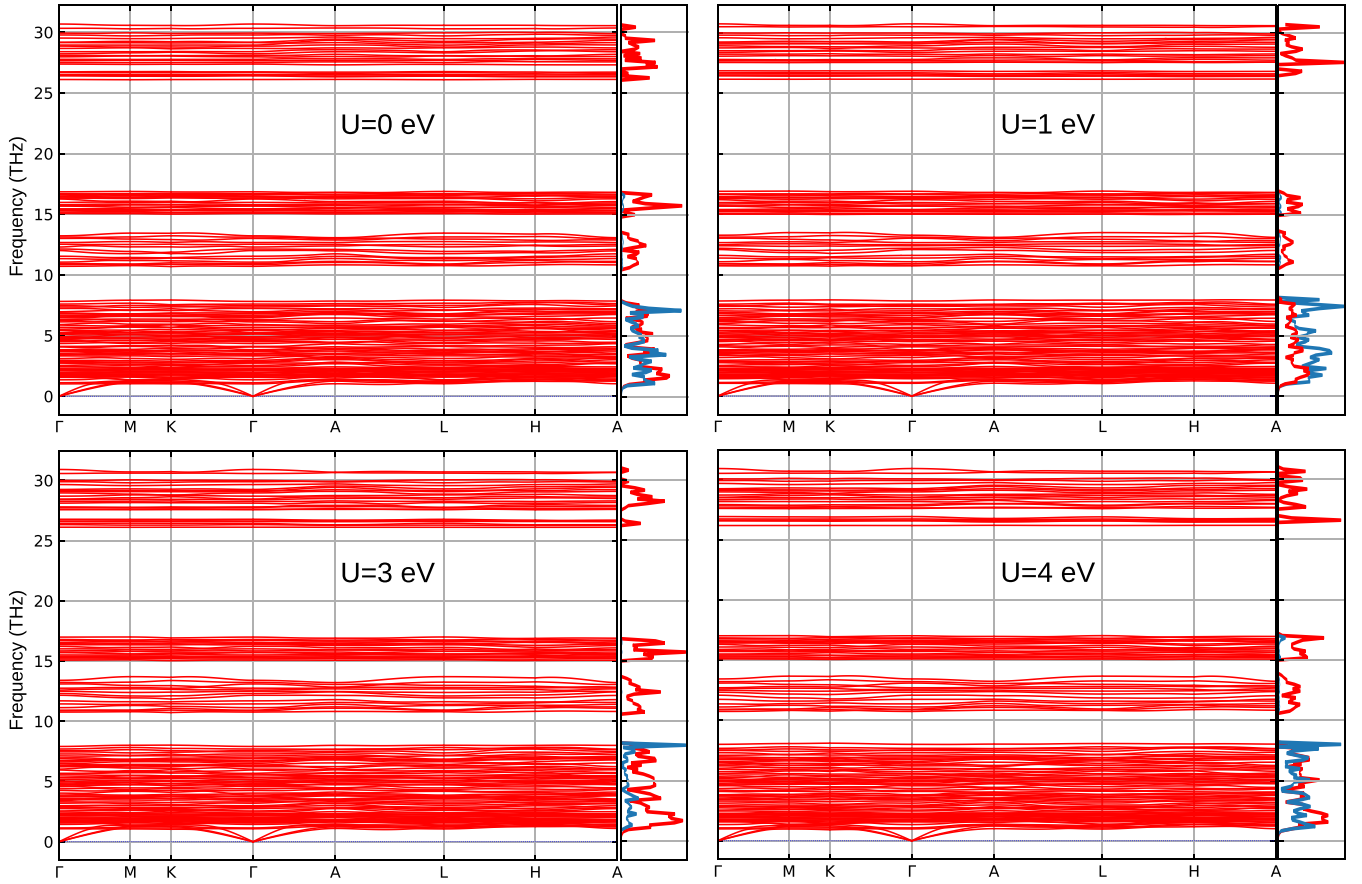
FIG. 17. Phonon band structure of the optimized geometry for different values of the Hubbard-like term U. The total (red) and partial (projected on Cu, blue) phonon densities of states are shown in the right panel in different scales.

APPENDIX A: FERMI SURFACE AND FERMI NESTING

The phonon self-energy can be written as

$$\Pi(\mathbf{q}, \omega) = -2 \sum_{\mathbf{k}, n, n'} \frac{f(\epsilon_{n,\mathbf{k}}) - f(\epsilon_{n',\mathbf{k}+\mathbf{q}})}{\epsilon_{n,\mathbf{k}} - \epsilon_{n',\mathbf{k}+\mathbf{q}} - \hbar\omega - i\delta} M^2_{n\mathbf{k}, n'\mathbf{k}+\mathbf{q}},$$

(A1)

where the band momentum and indexes are $\mathbf{k}$, n, and n', respectively. The occupation of a given state with energy ϵ is given by $f(\epsilon)$. The phonon momentum and energy are ω and $\mathbf{q}$. $M_{n\mathbf{k}, n'\mathbf{k}'}$ are the effective matrix elements of the deformation potential [83]. A divergence of the self-energy may arise at $\omega = 0$ if for a given vector $\mathbf{q}$ the bands are degenerate in a large region of the reciprocal space; in other words, the Fermi surfaces are nested.

Due to the difficulty in calculating M, it is often approximated as a constant, and the imaginary part of the bare electronic susceptibility with $\omega \to 0$, $\chi_0''(\mathbf{q})$, is used to quantify the Fermi nesting [46]:

$$\lim_{\omega \to 0} \frac{\chi_0''(\mathbf{q})}{\omega} = \sum_{n\mathbf{k}} \delta(\epsilon_{n,\mathbf{k}} - \epsilon_F) \delta(\epsilon_{n',\mathbf{k}+\mathbf{q}} - \epsilon_F),$$

(A2)

with ϵ_F being the Fermi energy. Although the calculation of the nesting can, in principle, be done with DFT [46,84], our attempt was impractical for a system this large that needs a dense grid of k points to describe its Fermi surface.

Instead of an actual calculation of $\chi_0''(\mathbf{q})$, in Fig. 12, we provide a section of the Fermi surface and the vectors $\mathbf{q}$ connecting two Fermi surfaces. Both Fermi surfaces have little dispersion near their crossing of the Γ-A line, favoring an overlap of $\epsilon_{\mathbf{k}}$ and $\epsilon_{\mathbf{k}+\mathbf{q}}$.

APPENDIX B: XRD

We ran a DFT machine-learned classical molecular dynamics simulation of this system at room temperature with a $3 \times 3 \times 3$ supercell (~1200 atoms; see Fig. 13). The calculated XRD pattern corresponds to the average along the last 500 fs of the simulation. In general, this is in good agreement with the experimental results. However, our peaks are shifted to larger angles, which is explained by the thermal expansion

of the lattice in our simulation. This picture agrees with a hexagonal lattice stabilized by temperature [25].

APPENDIX C: MACHINE LEARNING FORCE FIELDS

The training of a force field was performed on the fly: if the statistical uncertainty of the forces is above a certain threshold, the calculation is made with DFT; otherwise, the force field is used. This allows the use of DFT only as it is needed (i.e., new configurations outside the validity domain of the force field). The threshold to switch between DFT or the force field is defined on the fly to refine the force field accuracy along the calculation.

We started the training with a fixed lattice and low temperature. Then we allowed the lattice to relax to improve the force field. Finally, we increased the temperature to 400 K. Figure 14(a) shows the convergence of the Bayesian error in the forces for this last stage. For the simulation of a larger cell, we used only the force field; the statistical error in forces lies close to the training set [Fig. 14(b)]. It is worth noting that this level of error provides a qualitatively correct picture. For instance, the force field allowed us to identify the triclinic

structure as the minimum energy. A posterior relaxation with DFT of the triclinic structure resulted in minimal changes.

APPENDIX D: PROJECTED DENSITY OF STATES

We used the VASPKIT code [85] to obtain the projected density of states (PDOS) on the Cu atom in LK-99 with stacking A and an FM ground state from VASP calculated data. Figure 15 shows the PDOS of the s, p, and d orbitals of the Cu atom.

APPENDIX E: DEPENDENCE OF THE VALUE OF U

To explore the dependence of the calculations with respect to the Hubbard-like term U we calculated the band structure of the system in the hexagonal lattice with $U = 0-4$ eV (see Fig. 16). The changes close to the Fermi energy are minimal. However, the participation of Cu in the valence band (~ -1 eV) decreases when increasing the value of U.

The phonons of the triclinic lattice (see Fig. 17) are practically identical regardless of the value of U. The geometry was fully optimized for each U. The changes in the phonon density of states are likely due to the mesh size.

[1] H. K. Onnes, Further experiments with liquid helium. D. on the change of the electrical resistance of pure metals at very low temperatures, etc. V. The Disappearance of the resistance of mercury, in *Through Measurement to Knowledge*, Boston Studies in the Philosophy of Science, edited by K. Gavroglu and Y. Goudaroulis, Vol. 124 (Springer, Dordrecht, 1991), pp. 264–266.

[2] H. K. Onnes, Further experiments with liquid helium. C. On the change of electric resistance of pure metals at very low temperatures etc. IV. The resistance of pure mercury at helium temperatures, in *Through Measurement to Knowledge*, Boston Studies in the Philosophy of Science, edited by K. Gavroglu and Y. Goudaroulis, Vol. 124 (Springer, Dordrecht, 1991), pp. 261–263.

[3] J. Nagamatsu, N. Nakagawa, T. Muranaka, Y. Zenitani, and J. Akimitsu, Superconductivity at 39 K in magnesium diboride, Nature (London) **410**, 63 (2001).

[4] M.-K. Wu, J. R. Ashburn, C. Torng, P.-H. Hor, R. L. Meng, L. Gao, Z. J. Huang, Y. Wang, and A. Chu, Superconductivity at 93 K in a new mixed-phase Y-Ba-Cu-O compound system at ambient pressure, Phys. Rev. Lett. **58**, 908 (1987).

[5] S. Lee, J.-H. Kim, and Y.-W. Kwon, The first room-temperature ambient-pressure superconductor, arXiv:2307.12008.

[6] S. Lee, J. Kim, S. Im, S. An, Y.-W. Kwon, and K. H. Auh, Consideration for the development of room-temperature ambient-pressure superconductor (LK-99), J. Korean Cryst. Growth Cryst. Technol. **33**, 61 (2023).

[7] K. Kumar, N. Kumar Karn, Y. Kumar, and V. Awana, Absence of superconductivity in LK-99 at ambient conditions, ACS Omega **8**, 41737 (2023).

[8] Y. Zhang, C. Liu, X. Zhu, and H.-H. Wen, Ferromagnetism and insulating behavior with a logarithmic temperature dependence of resistivity in $Pb_{10-x}Cu_x(PO_4)_6O$, Sci. China: Phys., Mech. Astron. **67**, 217413 (2024).

[9] P. Wang, X. Liu, J. Ge, C. Ji, H. Ji, Y. Liu, Y. Ai, G. Ma, S. Qi, and J. Wang, Ferromagnetic and insulating behavior in both half magnetic levitation and non-levitation LK-99 like samples, Quantum Front. **2**, 10 (2023).

[10] M. Singh, P. Saha, K. Kumar, D. Takhar, B. Birajdar, V. Awana, and S. Patnaik, Electromagnetic properties of copper doped lead apatite $Pb_{10-x}Cu_x(PO_4)_6O$, J. Mater. Sci. **59**, 1464 (2024).

[11] P. K. Jain, Superionic phase transition of copper(i) sulfide and its implication for purported superconductivity of LK-99, J. Phys. Chem. C **127**, 18253 (2023).

[12] P. K. Jain, Solving the LK-99 puzzle, Matter **6**, 4118 (2023).

[13] C. Liu, W. Cheng, X. Zhang, J. Xu, J. Li, Q. Shi, C. Yuan, L. Xu, H. Zhou, S. Zhu, J. Sun, W. Wu, J. Luo, K. Jin, and Y. Li, Phases and magnetism at microscale in compounds containing nominal $Pb_{10-x}Cu_x(PO_4)_6O$, Phys. Rev. Mater. **7**, 084804 (2023).

[14] S. Zhu, W. Wu, Z. Li, and J. Luo, First-order transition in LK-99 containing Cu_2S, Matter **6**, 4401 (2023).

[15] T. Habamahoro, T. Bontke, M. Chirom, Z. Wu, J. M. Bao, L. Z. Deng, and C. W. Chu, Replication and study of anomalies in LK-99–the alleged ambient-pressure, room-temperature superconductor, Supercond. Sci. Technol. **37**, 045004 (2024).

[16] Z. Lei, C.-W. Lin, I.-N. Chen, C.-T. Chou, Y.-L. Lin, J.-H. Chen, H.-H. Sung, and L.-M. Wang, The characteristics of Cu-doped lead apatite (LK-99) synthesized with the removal of Cu_2S using ammonia solution: A diamagnetic semiconductor, APL Mater. **12**, 021104 (2024).

[17] B. Cho, J. Park, D. Yun, J. Seo, and K. Park, Exploration of superconductivity in LK-99 synthesized under different cooling conditions, Curr. Appl. Phys. **62**, 22 (2024).

[18] H. Chen, X. Zhou, Z. Meng, X. Wang, Z. Duan, L. Liu, G. Zhao, H. Yan, P. Qin, and Z. Liu, Magnetic-field response and giant electric-field modulation of Cu_2S, Nano Lett. **24**, 584 (2024).

[19] H. Wang *et al.*, Observation of diamagnetic strange-metal phase in sulfur-copper codoped lead apatite, arXiv:2403.11126.

[20] P. Abramian, A. Kuzanyan, V. Nikoghosyan, S. Teknowijoyo, and A. Gulian, Some remarks on possible superconductivity of composition $Pb_9CuP_6O_{25}$, Opt. Memory Neural Networks **32**, S424 (2023).

[21] J. Cao and A. Kavokin, The interplay between exciton- and phonon-induced superconductivity might explain the phenomena observed in LK-99, Mater. Today Commun. **37**, 107293 (2023).

[22] M. Y. Toriyama, C.-W. Lee, G. J. Snyder, and P. Gorai, Defect chemistry and doping of lead phosphate oxo apatite $Pb_{10}(PO_4)_6O$, ACS Energy Lett. **9**, 428 (2024).

[23] K. Tao, R. Chen, L. Yang, J. Gao, D. Xue, and C. Jia, The 1/4 occupied O atoms induced ultra-flatband and the one-dimensional channels in the $Pb_{10-x}Cu_x(PO_4)_6O$ ($x = 0, 0.5$) crystal, APL Mater. **12**, 021120 (2024).

[24] J. Shen, D. I. Gaines, S. Shahabfar, Z. Li, D. Kang, S. Griesemer, A. Salgado-Casanova, T.-C. Liu, C.-T. Chou, Y. Xia, and C. Wolverton, Phase stability of lead phosphate apatite $Pb_{10-x}Cu_x(PO_4)_6O$, $Pb_{10-x}Cu_x(PO_4)_6(OH)_2$ ($x = 0, 1$), and $Pb_8Cu_2(PO_4)_6$, Chem. Mater. **36**, 275 (2024).

[25] S.-W. Kim, K. Wang, S. Chen, L. J. Conway, G. L. Pascut, I. Errea, C. J. Pickard, and B. Monserrat, On the dynamical stability of copper-doped lead apatite, npj Comput. Mater. **10**, 16 (2024).

[26] J. Li and Q. An, Structural and electronic intricacies of Cu-doped lead apatite (LK-99): Implications for potential ambient-pressure superconductivity, J. Phys. Chem. C **128**, 580 (2024).

[27] M. Braß, L. Si, and K. Held, Weyl points and spin-orbit coupling in copper-substituted lead phosphate apatite, Phys. Rev. B **109**, 085103 (2024).

[28] S. M. Griffin, Origin of correlated isolated flat bands in copper-substituted lead phosphate apatite, arXiv:2307.16892.

[29] R. Kurleto, S. Lany, D. Pashov, S. Acharya, M. van Schilfgaarde, and D. S. Dessau, Pb-apatite framework as a generator of novel flat-band CuO based physics, including possible room temperature superconductivity, arXiv:2308.00698.

[30] J. Lai, J. Li, P. Liu, Y. Sun, and X.-Q. Chen, First-principles study on the electronic structure of $Pb_{10-x}Cu_x(PO_4)_6O$ ($x = 0, 1$), J. Mater. Sci. Technol. **171**, 66 (2024).

[31] L. Si and K. Held, Electronic structure of the putative room-temperature superconductor $Pb_9Cu(PO_4)_6O$, Phys. Rev. B **108**, L121110 (2023).

[32] L. Si, M. Wallerberger, A. Smolyanyuk, S. di Cataldo, J. M. Tomczak, and K. Held, $Pb_{10-x}Cu_x(PO_4)_6O$: A Mott or charge transfer insulator in need of further doping for (super)conductivity, J. Phys.: Condens. Matter **36**, 065601 (2024).

[33] Y. Sun, K.-M. Ho, and V. Antropov, Metallization and spin fluctuations in Cu-doped lead apatite, Phys. Rev. Mater. **7**, 114804 (2023).

[34] Y. Jiang, S. B. Lee, J. Herzog-Arbeitman, J. Yu, X. Feng, H. Hu, D. Călugăru, P. S. Brodale, E. L. Gormley, M. G. Vergniory, C. Felser, S. Blanco-Canosa, C. H. Hendon, L. M. Schoop, and B. A. Bernevig, $Pb_9Cu(PO_4)_6(OH)_2$: Phonon bands, localized flat-band magnetism, models, and chemical analysis, Phys. Rev. B **108**, 235127 (2023).

[35] D. M. Korotin, D. Y. Novoselov, A. O. Shorikov, V. I. Anisimov, and A. R. Oganov, Electronic correlations in the ultranarrow energy band compound $Pb_9Cu(PO_4)_6O$: A DFT + DMFT study, Phys. Rev. B **108**, L241111 (2023).

[36] H. Bai, J. Ye, L. Gao, C. Zeng, and W. Liu, Semiconductivity induced by spin–orbit coupling in $Pb_9Cu(PO_4)_6O$, Sci. Rep. **13**, 21085 (2023).

[37] L. Hao and E. Fu, First-principles calculation on the electronic structures, phonon dynamics, and electrical conductivities of $Pb_{10}(PO_4)_6O$ and $Pb_9Cu(PO_4)_6O$ compounds, J. Mater. Sci. Technol. **173**, 218 (2024).

[38] C. Yue, V. Christiansson, and P. Werner, Correlated electronic structure of $Pb_{10-x}Cu_x(PO_4)_6O$, Phys. Rev. B **108**, L201122 (2023).

[39] N. Witt, L. Si, J. M. Tomczak, K. Held, and T. O. Wehling, No superconductivity in $Pb_9Cu_1(PO_4)_6O$ found in orbital and spin fluctuation exchange calculations, SciPost Phys. **15**, 197 (2023).

[40] V. M. Bhatnagar, The mineral lead apatites, Bull. Mineral. **91.5**, 479 (1968).

[41] P. Alberius Henning, A. R. Landa-Cánovas, A. K. Larsson, and S. Lidin, Elucidation of the crystal structure of oxyapatite by high-resolution electron microscopy, Acta Cryst. Sect. B **55**, 170 (1999).

[42] J. D. Hopwood *et al.*, The identification and synthesis of lead apatite minerals formed in lead water pipes, J. Chem. **2016**, 1 (2016).

[43] S. V. Krivovichev and P. C. Burns, Crystal chemistry of lead oxide phosphates: Crystal structures of $Pb_4O(PO_4)_2$, $Pb_8O_5(PO_4)_2$ and $Pb_{10}(PO_4)_6O$, Z. Kristallogr. - Cryst. Mater. **218**, 357 (2003).

[44] S. Yang, G. Liu, and Y. Zhong, *Ab initio* investigations on the electronic properties and stability of Cu-substituted lead apatite (LK-99) family with different doping concentrations (x=0, 1, 2), Mater. Today Commun. **37**, 107379 (2023).

[45] S. B. Dugdale, Life on the edge: A beginner's guide to the Fermi surface, Phys. Scr. **91**, 053009 (2016).

[46] M. D. Johannes and I. I. Mazin, Fermi surface nesting and the origin of charge density waves in metals, Phys. Rev. B **77**, 165135 (2008).

[47] J. Hlinka, Possible ferroic properties of copper-substituted lead phosphate apatite, arXiv:2308.03691.

[48] A. D. Becke and K. E. Edgecombe, A simple measure of electron localization in atomic and molecular systems, J. Chem. Phys. **92**, 5397 (1990).

[49] T. Novoa, J. Contreras-García, P. Fuentealba, and C. Cárdenas, The Pauli principle and the confinement of electron pairs in a double well: Aspects of electronic bonding under pressure, J. Chem. Phys. **150**, 204304 (2019).

[50] A. Robles-Navarro, M. Rodriguez-Bautista, P. Fuentealba, and C. Cárdenas, The change in the nature of bonding in the Li_2 dimer under confinement, Int. J. Quantum Chem. **121**, e26644 (2021).

[51] E. Gull, A. J. Millis, A. I. Lichtenstein, A. N. Rubtsov, M. Troyer, and P. Werner, Continuous-time Monte Carlo methods for quantum impurity models, Rev. Mod. Phys. **83**, 349 (2011).

[52] M. P. Bahlke, M. Schneeberger, and C. Herrmann, Local decomposition of hybridization functions: Chemical insight into correlated molecular adsorbates, J. Chem. Phys. **154**, 144108 (2021).

[53] F. Belli, T. Novoa, J. Contreras-García, and I. Errea, Strong correlation between electronic bonding network and critical temperature in hydrogen-based superconductors, Nat. Commun. **12**, 5381 (2021).

[54] F. Giustino, Electron-phonon interactions from first principles, Rev. Mod. Phys. **89**, 015003 (2017).

[55] T. Yildirim, O. Gülseren, J. W. Lynn, C. M. Brown, T. J. Udovic, Q. Huang, N. Rogado, K. A. Regan, M. A. Hayward, J. S. Slusky, T. He, M. K. Haas, P. Khalifah, K. Inumaru, and R. J. Cava, Giant anharmonicity and nonlinear electron-phonon coupling in MgB$_2$: A combined first-principles calculation and neutron scattering study, Phys. Rev. Lett. **87**, 037001 (2001).

[56] H. Zhai, F. Munoz, and A. N. Alexandrova, Strain to alter the covalency and superconductivity in transition metal diborides, J. Mater. Chem. C **7**, 10700 (2019).

[57] W. Pickett, J. An, H. Rosner, and S. Savrasov, Role of two dimensionality in MgB$_2$, Phys. C (Amsterdam, Neth.) **387**, 117 (2003).

[58] R. H. Lavroff, J. Munarriz, C. E. Dickerson, F. Munoz, and A. N. Alexandrova, Chemical bonding dictates drastic critical temperature difference in two seemingly identical superconductors, Proc. Natl. Acad. Sci. USA **121**, e2316101121 (2024).

[59] To get a phonon involving the Cu displacement we calculate the vibrational modes of the Cu and its neighbor O atoms while keeping all other atoms fixed. We chose the mode with the largest Cu displacement to apply a frozen phonon. While the vibrational mode obtained this way is not an actual phonon, it can be expanded into the basis of the actual phonons of the system.

[60] S. Singh, A. H. Romero, J. D. Mella, V. Eremeev, E. Muñoz, A. N. Alexandrova, K. M. Rabe, D. Vanderbilt, and F. Muñoz, High-temperature phonon-mediated superconductivity in monolayer Mg$_2$B$_4$C$_2$, npj Quantum Mater. **7**, 37 (2022).

[61] A. B. Georgescu, Cu-doped Pb$_{10}$(PO$_4$)$_6$O, and V doped SrTiO$_3$ – a tutorial on electron-crystal lattice coupling in insulating materials with transition metal dopants, arXiv:2308.07295.

[62] P. Puphal, M. Y. P. Akbar, M. Hepting, E. Goering, M. Isobe, A. A. Nugroho, and B. Keimer, Single crystal synthesis, structure, and magnetism of Pb$_{10-x}$Cu$_x$(PO$_4$)$_6$O, APL Mater. **11**, 101128 (2023).

[63] G. Kresse and J. Hafner, *Ab initio* molecular dynamics for liquid metals, Phys. Rev. B **47**, 558 (1993).

[64] G. Kresse and J. Furthmüller, Efficiency of *ab initio* total energy calculations for metals and semiconductors using a plane-wave basis set, Comput. Mater. Sci. **6**, 15 (1996).

[65] G. Kresse and J. Furthmüller, Efficient iterative schemes for *ab initio* total-energy calculations using a plane-wave basis set, Phys. Rev. B **54**, 11169 (1996).

[66] G. Kresse and J. Hafner, *Ab initio* molecular-dynamics simulation of the liquid-metal–amorphous-semiconductor transition in germanium, Phys. Rev. B **49**, 14251 (1994).

[67] P. E. Blöchl, Projector augmented-wave method, Phys. Rev. B **50**, 17953 (1994).

[68] J. P. Perdew, K. Burke, and M. Ernzerhof, Generalized gradient approximation made simple, Phys. Rev. Lett. **77**, 3865 (1996).

[69] J. Heyd, G. E. Scuseria, and M. Ernzerhof, Hybrid functionals based on a screened Coulomb potential, J. Chem. Phys. **118**, 8207 (2003).

[70] A. V. Krukau, O. A. Vydrov, A. F. Izmaylov, and G. E. Scuseria, Influence of the exchange screening parameter on the performance of screened hybrid functionals, J. Chem. Phys. **125**, 224106 (2006).

[71] J. Paier, M. Marsman, K. Hummer, G. Kresse, I. C. Gerber, and J. G. Ángyán, Screened hybrid density functionals applied to solids, J. Chem. Phys. **124**, 154709 (2006).

[72] R. Jinnouchi, J. Lahnsteiner, F. Karsai, G. Kresse, and M. Bokdam, Phase transitions of hybrid perovskites simulated by machine-learning force fields trained on the fly with Bayesian inference, Phys. Rev. Lett. **122**, 225701 (2019).

[73] R. Jinnouchi, F. Karsai, and G. Kresse, On-the-fly machine learning force field generation: Application to melting points, Phys. Rev. B **100**, 014105 (2019).

[74] A. Togo and I. Tanaka, First principles phonon calculations in materials science, Scr. Mater. **108**, 1 (2015).

[75] A. Togo, First-principles phonon calculations with phonopy and phono3py, J. Phys. Soc. Jpn. **92**, 012001 (2023).

[76] A. Togo, L. Chaput, T. Tadano, and I. Tanaka, Implementation strategies in phonopy and phono3py, J. Phys.: Condens. Matter **35**, 353001 (2023).

[77] U. Herath, P. Tavadze, X. He, E. Bousquet, S. Singh, F. Muñoz, and A. H. Romero, Pyprocar: A Python library for electronic structure pre/post-processing, Comput. Phys. Commun. **251**, 107080 (2020).

[78] L. Lang, P. Tavadze, A. Tellez, E. Bousquet, H. Xu, F. Muñoz, N. Vasquez, U. Herath, and A. H. Romero, Expanding pyprocar for new features, maintainability, and reliability, Comput. Phys. Commun. **297**, 109063 (2024).

[79] A. M. Ganose, A. Searle, A. Jain, and S. M. Griffin, IFermi: A Python library for Fermi surface generation and analysis, J. Open Source Software **6**, 3089 (2021).

[80] S. L. Dudarev, G. A. Botton, S. Y. Savrasov, C. J. Humphreys, and A. P. Sutton, Electron-energy-loss spectra and the structural stability of nickel oxide: An LSDA+U study, Phys. Rev. B **57**, 1505 (1998).

[81] A. Jain, S. P. Ong, G. Hautier, W. Chen, W. D. Richards, S. Dacek, S. Cholia, D. Gunter, D. Skinner, G. Ceder, and K. A. Persson, Commentary: The Materials Project: A materials genome approach to accelerating materials innovation, APL Mater. **1**, 011002 (2013).

[82] K. Momma and F. Izumi, *VESTA* 3 for three-dimensional visualization of crystal, volumetric and morphology data, J. Appl. Cryst. **44**, 1272 (2011).

[83] W. E. Pickett and P. B. Allen, Superconductivity and phonon softening. III. Relation between electron bands and phonons in Nb, Mo, and their alloys, Phys. Rev. B **16**, 3127 (1977).

[84] H. Lee, S. Poncé, K. Bushick, S. Hajinazar, J. Lafuente-Bartolome, J. Leveillee, C. Lian, F. Macheda, H. Paudyal, W. H. Sio, S. Tiwari, M. Zacharias, X. Zhang, N. Bonini, E. Kioupakis, E. R. Margine, and F. Giustino, Electron-phonon physics from first principles using the EPW code, npj Comput. Mater. **9**, 156 (2023).

[85] V. Wang, N. Xu, J.-C. Liu, G. Tang, and W.-T. Geng, VASPKIT: A user-friendly interface facilitating high-throughput computing and analysis using vasp code, Comput. Phys. Commun. **267**, 108033 (2021).